Heterojunctions in g-C3N4/TiO2(B) nanofibres with exposed (001) plane and enhanced visible-light photoactivity

Author

Zhang, Lin, Jing, Dengwei, She, Xilin, Liu, Hongwei, Yang, Dongjiang, Lu, Yun, Li, Jian, Zheng, Zhanfeng, Guo, Liejin

Published

Journal Title

DOI

Copyright Statement

Downloaded from

Griffith Research Online

Heterojunctions in g-C$_3$N$_4$/TiO$_2$(B) Nanofibres with Exposed (001) Plane and Enhanced Visible-Light Photoactivity

Lin Zhang,[a] Dengwei Jing,[b] Xilin She,[a] Hongwei Liu,[c] Dongjiang Yang, [a,c,][*] Yun Lu,[d] Jian Li,[d] Zhanfeng Zheng,[e,][*] and Liejin Guo[b]

The formation of heterojunctions is an e 97542fficient strategy to extend the light response range of TiO$_2$-based catalysts to visible light region. In addition to the bandgap edge match between the narrow bandgap semiconductors and the TiO$_2$ substrate, a stable phase interface between the sensitiser and TiO$_2$ is crucial for the construction of heterojunctions, since it acts as a tunnel for the efficient transfer of photogenerated charges. Herein, the coincidence site density (1/Σ) of graphite-like carbon nitride (g-C$_3$N$_4$) nanoflakes and two types of TiO$_2$ nanofibres [anatase and TiO$_2$(B)] was calculated by near coincidence site lattice (NCSL) theory. It was found that the coincidence site density of g-C$_3$N$_4$ and TiO$_2$(B) nanofibre with exposed (001) plane is 3 times of that of the g-C$_3$N$_4$ and anatase nanofibre with exposed (100) plane. This indicated that the g-C$_3$N$_4$ nanoflakes are more favourite to form stable heterojunctions with TiO$_2$(B) nanofibres. As expected, stable phase interface was formed between the plane of (22-40) of g-C$_3$N$_4$ and the plane (110) of TiO$_2$(B) which had same d-spacing of 0.35 nm and same orientation. Under visible light irradiation, the g-C$_3$N$_4$/TiO$_2$(B) system exhibited better photodegradation ability for sulforhodamine B (SRB) dye than g-C$_3$N$_4$/anatase system, although the photoactivity of the anatase nanofibres was much better than that of the TiO$_2$(B) nanofibres. Apparently, the phase interface between g-C$_3$N$_4$ and TiO$_2$(B) was more favourable for the electron transfer, which means that the g-C$_3$N$_4$ flakes were easier to sensitise the TiO$_2$(B) nanofibres rather than the traditional anatase phase.

1 Introduction

Titanium dioxide (TiO$_2$) has attracted much attention due to its superior chemical stability, large surface area, high activity, commercial availability, nontoxicity and so on.[1-3] It has been extensively used in photocatalysis,[4, 5] solar cells,[6] UV shield, paints and cosmetics.[7] Among these fields, TiO$_2$ is considered to be one of the most promising semiconductor photocatalysts for controlling the environmental pollutants, especially for organic pollutants in air or wastewater.[8, 9] However, TiO$_2$ is only excited by UV light with wavelength less than 387.5 nm due to its wide bandgap. Unfortunately, UV light (under 400 nm) only accounts for 3%~5% in sunlight, which leads to low solar energy conversion efficiency.[3, 10, 11] During the past decade, great effort has been devoted to modifying TiO$_2$, including hydrogenation modified TiO$_2$,[12, 13] energy band modulation by doping with metal elements such as Fe, Cr, Co, Ni and Cu[14-18] and non-metal elements such as N, C, P, B, F, and S.[10, 19-24] It is believed that bulk doping or matrix substitution can introduce interior electron states within the band gap and thus shift the response to the visible region. Recently, the grafting of optimal trace silica on anatase substrates can produces surface electronic states within the TiO$_2$ band gap, and thus can significantly enhance their photocatalytic activity for decomposing organic contaminants.[25] Furthermore, the construction of heterojunctions by combining TiO$_2$ with other semiconductors with narrow bandgap is another efficient pathway to extend the visible light response of TiO$_2$-based catalysts. Similar to the dye sensitised TiO$_2$,[26-28] the heterojunctions are responsible for an efficient photogenerated charge transfer from narrow band gap semiconductors to the TiO$_2$ substrate, which is crucial for increasing the activity of semiconductor-based photocatalysts.[29-31] Besides the bandgap match between the sensitiser and the TiO$_2$, the phase interface between the sensitiser and the TiO$_2$ is significant since the interface is the channel to transfer the photogenerated carriers to the surface of the TiO$_2$ substrate from the sensitiser.[32-34]

Recently, polymeric graphitic carbon nitride materials (g-C$_3$N$_4$) have emerged as a new class of photocatalyst owing to its visible-light driven bandgap (2.69 eV) and high stability. More importantly, the highest occupied molecular orbital (HOMO) of the g-C$_3$N$_4$ is located at -1.12 eV and is more negative than the conduction band (CB) of the common wide bandgap semiconductor photocatalysts such as TiO$_2$, ZnO, and BiPO$_4$, which is favourable to form heterojunctions with these wide bandgap semiconductors and thus to extend their visible light response. For instance, core/shell structured g-C$_3$N$_4$/BiPO$_4$ photocatalyst displayed superior photodegradation activity for MB dye under UV or visible light irradiation than pure C$_3$N$_4$ or BiPO$_4$ catalyst, since match of lattice and bandgap edge potential between the C$_3$N$_4$ and BiPO$_4$ results in the formation of heterojunctions. In addition, g-C$_3$N$_4$ was mixed with TiO$_2$ to fabricate hybrid photocatalysts via hydrothermal or thermal treatment. These hybrid photocatalysts have displayed high

photoactivity for phenol degradation and water splitting. However, only anatase was usually utilised to assemble with g-C$_3$N$_4$ since it is the most photoactive phase among the four common TiO$_2$ polymorphs [four polymorphs in nature: anatase(tetragonal, space group I4$_1$/amd), rutile(tetragonal, space group P4$_2$/mnm), brookite (orthorhombic, space group Pbca), and TiO$_2$(B) (monoclinic, space group C2/m)][33], and to date no studies of heterojunctions between g-C$_3$N$_4$ and other TiO$_2$ phases such as rutile, brookite, and TiO$_2$(B) have been reported. Particularly, TiO$_2$(B), a metastable monoclinic modification of TiO$_2$, is less active than anatase under UV light irradiation due to the existence of numerous defects, although it possesses narrower bandgap than antase phase[33].

In this study, in order to search a better TiO$_2$ candidate to load g-C$_3$N$_4$ sensitiser, the near coincidence site lattice (NCSL) theory was employed to calculate the coincidence site density of g-C$_3$N$_4$ nanoflakes and TiO$_2$(B) nanofibres with exposed (001) plane and anatase nanofibres with exposed (100) plane, which could be used for the guidance for the fabrication of new nanocomposite catalyst. It was found the coincidence site density of the g-C$_3$N$_4$/TiO$_2$(B) system is much higher than that of the system composed of g-C$_3$N$_4$ and anatase nanofibres with exposed (100) plane, which means the g-C$_3$N$_4$/TiO$_2$(B) system is more favourite to form stable heterojunctions. And as expected, the g-C$_3$N$_4$/TiO$_2$(B) system exhibited better photodegradation ability for sulforhodamine B (SRB) dye than g-C$_3$N$_4$/anatase system under visible light irradiation, although the photoactivity of pure anatase is much better than that of the pure TiO$_2$(B) phase.

2 Experiment section

2.1 Materials synthesis

Synthesis of TiO$_2$(B) nanofibres. TiO$_2$(B) nanofibres were prepared using a hydrothermal method combined with a subsequent calcination process.[35-37] In the typical hydrothermal process, 5 g of anatase TiO$_2$ powder (~325 mesh from Aladdin) was mixed with 70 ml of 10 M NaOH solution. The suspension were sonicated in an ultrasonic bath for 0.5 h and then transferred into an autoclave with a PTFE container inside. The autoclave was maintained at hydrothermal temperature of 180 °C for 48 h. The precipitate (sodium titanate nanofibres) was recovered, washed with distilled water (to remove excess NaOH), exchanged with H$^+$ (using a 0.1 M HCl solution) to produce H$_2$Ti$_3$O$_7$ nanofibres, and washed again with distilled water until pH~7 was reached. The H$_2$Ti$_3$O$_7$ nanofibre product was dried at 80 °C for 12 h. The oven-dried samples were calcined in muffle furnace at 450 °C for 4h in an air atmosphere. Thus, TiO$_2$(B) nanofibres were finally obtained. For comparison, anatase nanofibres [TiO$_2$(A)] were prepared by calcining H$_2$Ti$_3$O$_7$ nanofibres at 700 °C for 4 h.

Synthesis of g-C$_3$N$_4$. The g-C$_3$N$_4$ was prepared by heating melamine (Aladdin) in a muffle furnace at 550 °C for 4 h. After naturally cooled to room temperature, g-C$_3$N$_4$ with a faint yellow colour was obtained.

Fabrication of g-C$_3$N$_4$/TiO$_2$ hybrid photocatalyst. A typical synthesis of g-C$_3$N$_4$/TiO$_2$ hybrid photocatalyst was as follows: Firstly, an appropriate amount of g-C$_3$N$_4$ was added into methanol (Aladdin) in a beaker and then the beaker was placed in an ultrasonic bath for 30 min to completely disperse the g-C$_3$N$_4$.

After the ultrasonic process, the g-C$_3$N$_4$ particles were exfoliated to nanoflake structures. The TiO$_2$(B) nanofibres were added into the above solution and stirred in a fume hood for 24 h. After volatilisation of the methanol, an opaque powder was obtained after drying at 100 °C. After that, the powders were collected and calcined at 300 °C for 2h in an air atmosphere to make a firm connection between g-C$_3$N$_4$ and TiO$_2$(B) nanofibres. According to this method, different mass ratios of g-C$_3$N$_4$/TiO$_2$(B) photocatalysts at 0.5%, 1%, 3%, and 5% were synthesised and labelled as g-C$_3$N$_4$/TiO$_2$(B)-0.5, g-C$_3$N$_4$/TiO$_2$(B)-1, g-C$_3$N$_4$/TiO$_2$(B)-3, g-C$_3$N$_4$/TiO$_2$(B)-5, respectively. For comparison, the g-C$_3$N$_4$/TiO$_2$(A) nanofibre catalysts were fabricated by using the same method.

Photoelectrode preparation. Commercialized ITO was used in the present study, The ITO glass was of 15 mm × 10 mm in size. The ITO glass was first ultrasonically cleaned with acetone of analytical grade for 5 min, rinsed with deionized water, and then dried with a clean, dry airflow. One longitudinal edge of the conductive side was then carefully covered with insulating tape and the exposed effective area of the ITO glass was 10 mm × 10 mm. 20 mg of g-C$_3$N$_4$/TiO$_2$(B) powder was mixed with 0.1 mL of deionized water and 30 μL diacetone in an agate mortar, and the mixture was carefully ground for 10 min to form a homogeneous suspension. Then, 0.025 ml of the as-prepared suspension was evenly distributed onto the exposed area of the conductive side of the ITO glass. The susoension was then evenly spread over the exposed effective area of the ITO glass. The insulating tape on the edge of the ITO glass was removed after the suspension had dried in the air. Finally, the ITO glass deposited with the as-prepared suspension was heated to 300℃ for 2h under vacuum condition. A copper wire was connected to the conductive side of the ITO glass using conductive silver tape. Uncoated parts of the conductive side of the ITO glass were isolated with parafilm after the conductive silver tape had dried

2.2 Characterisations

Microscopic morphology of the samples was observed by scanning electron microscopy (SEM, FEI, Quanta 200) and transmission electron microscopy (TEM, FEI, Tecnai G20). Chemical compositions were characterised by energy dispersive spectroscopy (EDS, attached to the SEM). Crystalline structures were identified by X-ray diffraction (XRD, DX2700, China) operating with Cu Kα radiation (λ = 1.5418 Å) at a scan rate (2θ) of 2°/min with the accelerating voltage of 40 kV and the applied current of 30 mA, ranging from 5° to 80°. UV-Vis diffuse reflectance spectra (DRS) were recorded on a spectrophotometer (PE, Lambda35). Photoluminescence spectra (PL) of the samples were obtained using a Cary Eclipse Fluorescence spectrophotometer (Varian Company, Australia) at room temperature.

2.3 Photoelectrochemical measurement

A three-electrode system was employed to measure the varations of the photoinduced current density with time (i-t curve) of the prepared photoelectrodes using the CHI Electrochemical Workstation (CHI 760C, Shanghai Chenhua, China). The photoelectrodes (1 cm×1 cm), Ag/AgCl, and platinum electrode acted as the working, reference and counter electrodes, respectively.The electrolyte was 0.5 M NaSO$_4$. A 300 W Xe

illuminator (Peking Changtuo, PLS- 3XE300) with a cutoff filter to remove light of wavelengths below 420 nm was used as the visible light source. The electrodes were irradiated from the back side (ITO substrate/semiconductor interface). The i-t curves were measured at a 0 V bias potential.

2.4 Evaluation of photocatalytic activity

The photocatalytic activity of g-C_3N_4/TiO_2(B) were evaluated by photodegradation of sulforhodamine B (SRB) in a reactor with a volume of 100 ml under visible light irradiation. The irradiation source is a 108 w lamp (Philips) with a wavelength of > 400nm. The photocatalytic activities of the samples judged by measuring the loss of SRB in aqueous solution. The initial volume and concentration of SRB was 35 ml and 25 μmol L^{-1}, respectively. Before the light was turned on, the solution was stirred in dark for 30 minutes to ensure adsorption equilibrium between the catalyst and the dye. During the photocatalytic reaction, about 5 millilitres of samples were taken at one hour intervals and separated through centrifugation (12000 rpm, 5min). The concentration of SRB was analysed by recording variations of the absorption band maximum in the UV-Vis spectra of SRB using a UV-3200PC spectrophotometer (Kamada, China).

3 Results and discussion

3.1 Crystallographic orientation relationships between TiO_2(B) and g-C_3N_4

Orientation relationship between TiO_2(B) and g-C_3N_4 was investigated by using near coincidence site lattice (NCSL) theory. NCSL is a super lattice at the interface between two adjacent phases and is the structure of the interface. The NCSL is two-dimensional periodic lattice with a certain symmetry and a certain coincidence site density (1/Σ) which is proportional to the system energy. Σ is the multiplicity of the unit cell. The crystal structure parameters of TiO_2(B), anatase and g-C_3N_4 are shown in Table S1, where anatase phase was provided for comparison. According to TEM experimental investigation (Fig. S1), the exposed plane of TiO_2(B) nanofibre is (001) and that of anatase is (100). The calculation of the NCSL lattice between TiO_2 nanofibre and g-C_3N_4 was conducted based on these crystal structure parameters (Scheme S1) and listed in Table S2.

Obviously, the coincidence site multiplicity (Σ) of g-C_3N_4/TiO_2(B) system is 7, which is much lower than that of g-C_3N_4/anatase system (23). This means the g-C_3N_4/TiO_2(B) system is more favourite and stable. As shown in Scheme S1C, it could be predicted that a rotation angle of θ=17.4° must be achieved between TiO_2(B) and g-C_3N_4 phases if the g-C_3N_4 phase is able to superimpose over the super lattice of TiO_2(B). Fortunately, the departure angle of plane (110) and (020) is exactly 17.4°. This is the induced angle between [010] of TiO_2(B) nanofibre and [2-1-10] of g-C_3N_4 phase, which suggests that a pair of planes parallel and sharing same planar spacing should exist between TiO_2(B) and g-C_3N_4 phases. As illustrated in Scheme 1A, g-C_3N_4 shows perfect two-dimensional 6-fold symmetry with hollow tunnels and the lattice parameter of a=0.246 nm. TiO_2(B) crystal has a C-centred monoclinic structure with space group C2/m and the lattice parameter of a= 1.196 nm, b=0.374 nm (Scheme 1B). As shown in Scheme 1C, viewed at [001] direction of TiO_2(B), plane (110) is edge on and has a

lattice spacing of 0.35 nm which is equal to that of plane (22-40) of g-C_3N_4. Apparently, a perfect planar matching exists between plane (110) of TiO_2(B) and plane (22-40) of g-C_3N_4, which means stable heterojunctions are easily formed by annealing g-C_3N_4 phase on the surface of TiO_2(B) nanofibres with exposed (001) plane.
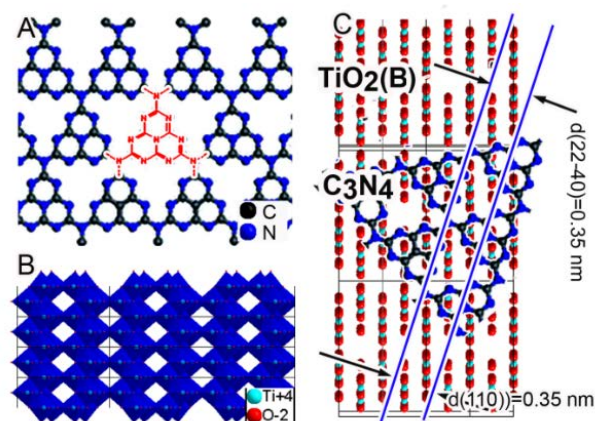
Scheme 1. Crystal model and oriented attachment of g-C_3N_4/TiO_2(B) system. (A) Atom configuration of g-C_3N_4 viewed along Z direction (i.e. [0001]). (B) Crystal structure of TiO_2(B) viewed along [001] direction. (C) Preferred orientation relationship between g-C_3N_4 and TiO_2(B).

3.2 SEM, TEM, and XRD of g-C_3N_4/TiO_2(B) nanofibres

The SEM images of the g-C_3N_4/TiO_2(B) hybrids are displayed in Fig. 1. For comparison, the images of pure g-C_3N_4 and TiO_2(B) nanofibre are also provided. As shown in Fig. 1A, the g-C_3N_4 sample is composed of lamellar microscaled particles with irregular shapes before ultrasonic treatment. The pure TiO_2(B) nanofibres are about 3-5 μm long and 200~300 nm wide (Fig. 1B). When the g-C_3N_4 was treated by ultrasound, the lamellar g-C_3N_4 particles could be disassembled into nanoflakes (or nanosheets).[38] These nanoflakes could be annealed onto the surface of the TiO_2(B) nanofibres after calcination at 300 °C. The SEM image of g-C_3N_4/TiO_2(B)-1 which contains 1 % g-C_3N_4 is presented in Fig. 1C. Apparently, compared with the pure TiO_2(B) nanofibres, the surface of the TiO_2(B) nanofibres in the g-C_3N_4/TiO_2(B)-1 hybrid became rough due to the introduction of g-C_3N_4 nanoflakes. When the g-C_3N_4 content increases to 5% (Fig. 1D), the roughness of the TiO_2(B) nanofibres in the g-C_3N_4/TiO_2(B)-5 hybrid was much larger than those of the nanofibres in g-C_3N_4/TiO_2(B)-1 hybrid and pure TiO_2(B) nanofibres. The introduction of g-C_3N_4 was also verified by the EDS spectra (insets in Fig. 1). Besides the signals of titanium and oxygen elements which are from the TiO_2(B) nanofibres, the signals of carbon and nitrogen elements could be probed from the spectra of g-C_3N_4/TiO_2(B)-1 and g-C_3N_4/TiO_2(B)-5, indicating that the g-C_3N_4 has been successfully coated on the surface of TiO_2(B) nanofibres through the simple ultrasonic dispersion and calcination process.
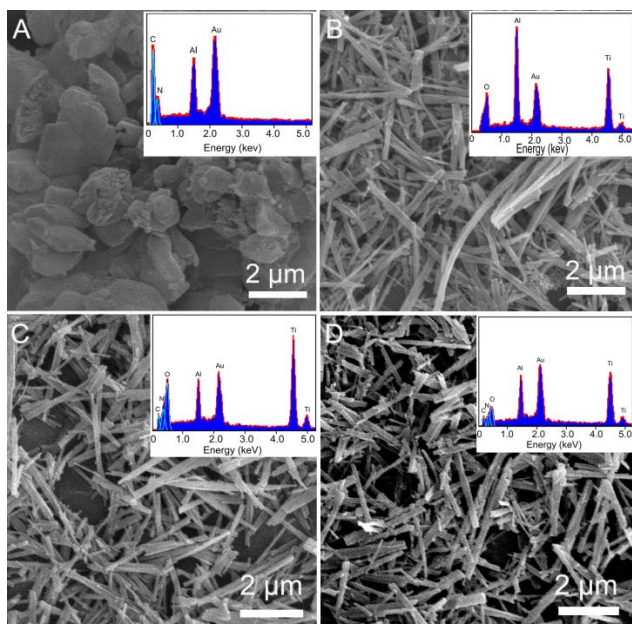
Fig. 1 The scanning electron microscope (SEM) images of (A) g-C_3N_4 without ultrasonic treatment, (B) pristine TiO_2(B) nanofibres, (C) g-C_3N_4/TiO_2(B)-1, and (D) g-C_3N_4/TiO_2(B)-5. Insets: the EDS spectra of the samples. The signals of gold and aluminium are originated from the coating layer and aluminium foil used for SEM observation.
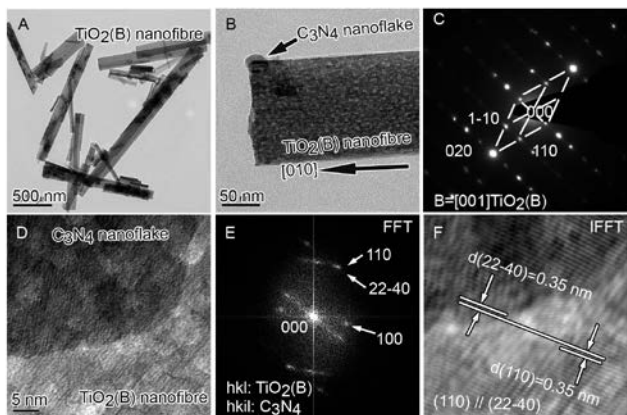

Fig. 2 (A)(B) TEM images of the g-C_3N_4/TiO_2(B)-1 photocatalyst, (C) electron diffraction pattern (EDP) of the g-C_3N_4/TiO_2(B)-1 photocatalyst, (D) HRTEM image of a g-C_3N_4 nanoflake deposited on the TiO_2(B) nanofibre, (E) fast flourier transformation (FFT) image of the joint area between g-C_3N_4 and TiO_2(B) in image D, (F) inverse fast flourier transformation (IFFT) image.

Fig. 2 displays the typical TEM images of the g-C_3N_4/TiO_2(B)-1 photocatalyst. As expected, the g-C_3N_4 particles converted into nanoflakes after the ultrasonic process, and these flakes were coated on the TiO_2(B) nanofibres during the subsequent annealing treatment at 300 °C. Fig. 2A is the TEM bright field image of TiO_2(B) nanofibres attached with small amount of g-C_3N_4 nanoflakes, and a higher magnification TEM bright field image in Fig. 2B shows a fragment of g-C_3N_4 on a single TiO_2(B) nanofibre growing along [010] direction. The electron diffraction pattern (EDP) of a single TiO_2(B) nanofibre was taken down [001] direction (Fig. 2C). The diffraction spots could be indexed as (110), (1-10), and (020). The high-resolution TEM (HRTEM) image of the joint area between g-C_3N_4 and TiO_2(B) nanofibre is depicted in Fig. 2D. Its fast Flourier transformation (FFT)

provided electron diffraction signals from g-C_3N_4 and TiO_2(B) phases in the joint area (Fig. 2E). The corresponding fast Flourier transformation (IFFT) in Fig. 2F confirmed that plane of (22-40) of g-C_3N_4 was parallel to plane (110) of TiO_2(B). Given that both planes have the same *d*-spacing of 0.35 nm and the same orientation, the g-C_3N_4 flakes tended to extend across the adjacent interface and grow firmly with the TiO_2(B) nanofibres. This is in good agreement with the calculated results from NCSL theory.
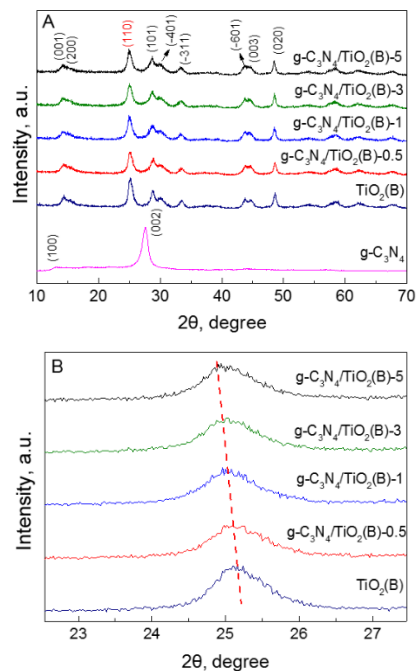

Fig. 3 XRD patterns of pure TiO_2(B) nanofibres and g-C_3N_4/TiO_2(B) prepared with different mass ratio of g-C_3N_4 to TiO_2 (M_{g-C3N4}:$M_{TiO2(B)}$ = 0.5%, 1%, 3%, and 5%, respectively).

The XRD patterns of the TiO_2(B) nanofibres annealed with different mass ratio of g-C_3N_4 nanoflakes were presented in Fig. 3. Compared with the g-C_3N_4 nanoflakes, the TiO_2(B) nanofibres possess higher crystallinity. So only the diffraction peaks of TiO_2(B) phase were observed from the patterns. However, the diffraction peaks of TiO_2(B) phase decrease slightly with the introduction of g-C_3N_4. And as shown in Fig. 3B, the diffraction peak of the plane (110) of TiO_2(B) shifted slightly to the smaller value of the diffraction angle with the attachment of the g-C_3N_4 nanoflakes.

3.3 DRS, photoelectrochemical test and PL spectra

The optical absorption properties of the hybrid g-C_3N_4/TiO_2(B) nanofibres were investigated by UV–Vis diffuse reflectance spectroscopy (DRS). Fig. 4A shows the DRS spectra of the hybrid g-C_3N_4/TiO_2(B) photocatalysts. As can be seen clearly, g-C_3N_4 was able to absorb light with wavelength up to 450 nm. The absorption wavelength of TiO_2(B) nanofibres was under 400 nm which means pure TiO_2(B) could only have a response to UV light. After coupled with g-C_3N_4 nanoflakes, the hybrid g-C_3N_4/TiO_2(B) nanofibres display more efficient light absorption from 400 nm to 800 nm in comparison with the pure TiO_2(B) nanofibre (Fig. 4B), although the trace amount of g-C_3N_4 could

not result in the absorption edge shift. This means that the g-C_3N_4 nanoflakes could act as a visible light sensitiser to drive a reaction on the surface of the TiO_2(B) nanofibres. Additionally, the g-C_3N_4/TiO_2(B) nanofibres inherited the obvious light
5 absorption in the UV light region from the pristine TiO_2(B) nanofibres, which could make up the weak absorption of UV light by g-C_3N_4. This is crucial for a visible light photocatalyst to efficiently absorb and utilise the UV light (3% ~ 5%) in sunlight. The photoelectrochemical test (Fig. 5) shows that after g-C_3N_4 is
10 attached to the surface of TiO_2, there is a clear increase of the photogenerated current density. These further confirms that there is a strong interaction between the two phases of the g-C_3N_4/TiO_2(B) hybrid material. The room temperature photoluminescence (PL) spectra of g-C_3N_4/TiO_2(B) nanofibres
15 and pure g-C_3N_4 and TiO_2(B) nanofibres are compared in Fig. S5. The g-C_3N_4/TiO_2 hybrid nanofibres and g-C_3N_4 exhibit much weaker florescence than g-C_3N_4.
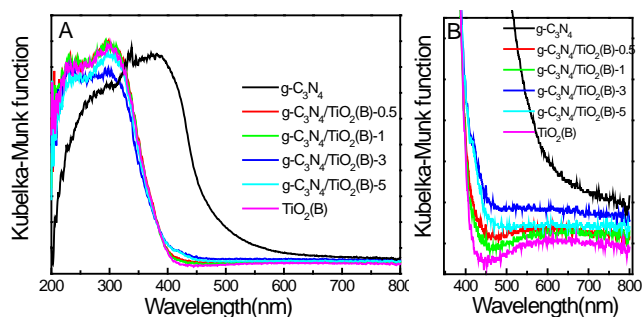

Fig. 4 (A) UV-Vis diffuse reflection spectra of TiO_2(B), g-C_3N_4, and g-
20 C_3N_4/TiO_2(B) samples. (B) The enlarged absorption between 350 and 800 nm of the spectra in panel A.
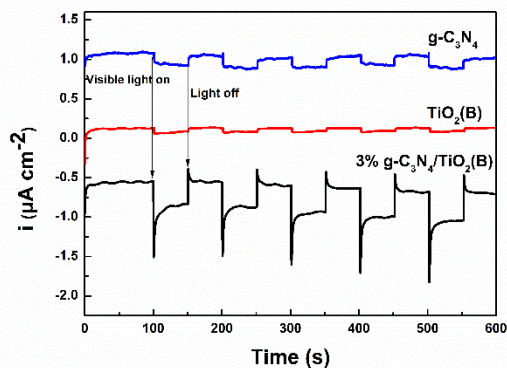

Fig. 5 Photogenerated current densities of the g-C_3N_4, TiO_2(B), and 3% g-C_3N_4/ TiO_2(B). All the curves were obtained at 0V bias potential under
25 visible light on and off.

3.4 Photocatalytic properties of g-C_3N_4/TiO_2(B) nanofibres

The photocatalytic activity of the g-C_3N_4/TiO_2(B) samples was evaluated by degradation of sulforhodamine B (Aldrich). Fig. 6A shows the SRB photodegradation by the g-C_3N_4/TiO_2(B) samples
30 with different g-C_3N_4 content under visible light irradiation. Apparently, it can be observed that all g-C_3N_4/TiO_2(B) photocatalysts exhibited higher photoactivity than pure g-C_3N_4 and TiO_2(B) under visible light irradiation, particularly the g-C_3N_4/TiO_2(B)-1 photocatalyst. For instance, after 5 h visible light
35 irradiation, the removal efficiency of SRB was 43.4, 56.3, 22.5,

and 19.5% for g-C_3N_4/TiO_2(B)-0.5, g-C_3N_4/TiO_2(B)-1, g-C_3N_4/TiO_2(B)-3, and g-C_3N_4/TiO_2(B)-5, respectively. The photodegradation efficiency was much higher than that of the pure g-C_3N_4 (16.7 %) and TiO_2(B) nanofibres (14.8 %). To
40 further depict the photocatalytic reaction, the kinetics of the degradation reaction was fitted to a pseudo-fist-order rate law using the equation ln $(C_0/C) = k$, where k is the apparent rate constant with determined irradiation time, C_0 is the initial concentration of SRB and C is the instantaneous concentration.[39]
45 The value of the rate constant k is equal to the corresponding slope of the fitting line, as can be seen in Fig. 6B. The k value for g-C_3N_4/TiO_2(B)-1 was 0.1252 h^{-1}, which was almost 5.09, 4.96, 1.58, 3.3, and 3.4 times as high as that of the pristine TiO_2(B) nanofibres, pure g-C_3N_4 particles, g-C_3N_4/TiO_2(anatase)-0.5, g-
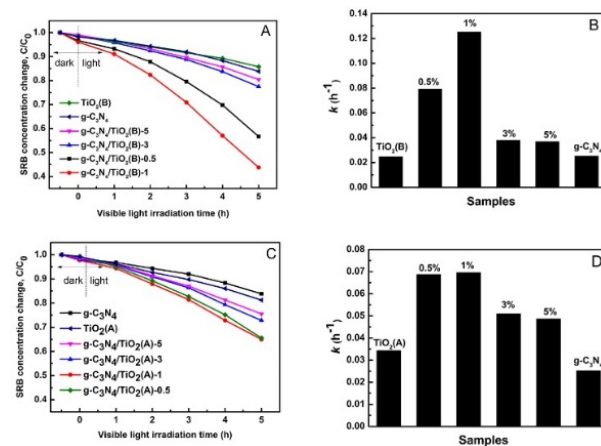50 C_3N_4/TiO_2(anatase)-3, and g-C_3N_4/TiO_2(anatase)-5, respectively.

Fig. 6 (A) Photocatalytic degradation of SRB (C_0 = 25 μmol L^{-1}) under visible light irradiation. (B) Average reaction rate constants k for photodegradation of SRB over g-C_3N_4/TiO_2(B) samples with different
55 mass ratios. (C), (D) The SRB degradation curves and average reaction rate constants k for g-C_3N_4/anatase photocatalysts which were prepared using the same method.

For comparison, the photoactivity for the degradation of SRB by g-C_3N_4/anatase nanofibres was investigated. As shown in Fig.
60 6C, the pure anatase nanofibres [TiO_2(A)] could decompose 18.7 % of the SRB dye after 5 h visible light irradiation, which is higher than that of the TiO_2(B) nanofibres. However, the removal efficiencies of SRB of the hybrid g-C_3N_4/TiO_2(A) catalysts were much lower than those of the g-C_3N_4/TiO_2(B) catalysts. For
65 example, the most active g-C_3N_4/TiO_2(A)-1 could decompose 35.5 % of the SRB dye, much lower than that of the g-C_3N_4/TiO_2(B)-1 (56.3%). Similar results were obtained from the apparent rate constant values of the g-C_3N_4/TiO_2(A) catalysts (Fig. 5D). Obviously, the g-C_3N_4/TiO_2(B) nanofibres possessed
70 superior photocatalytic activity to that of g-C_3N_4/TiO_2(A) ones under visible light irradiation

The photoactivity of the TiO_2(B) nanofibres modified with the optimal quantity of g-C_3N_4 under UV light irradiation was also investigated by the degradation of SRB dye. As shown in Fig. S3,
75 the g-C_3N_4/TiO_2(B) nanofibres displayed higher photoactivity for the degradation of SRB dye under the UV light irradiation than the pristine TiO_2(B) nanofibres and g-C_3N_4. The k values are 1.76, 1.83, 1.73, and 2.03 h^{-1} for g-C_3N_4/TiO_2(B)-0.5, g-C_3N_4/TiO_2(B)-1, g-C_3N_4/TiO_2(B)-3, and g-C_3N_4/TiO_2(B)-5,

respectively, higher than that of pristine $TiO_2(B)$ nanofibres (1.50) and pure g-C_3N_4 (0.402). Apparently, the g-C_3N_4/$TiO_2(B)$ catalysts still maintained a high photocatalytic activity under UV irradiation.

3.5 Proposed charge transfer in g-C_3N_4/$TiO_2(B)$ nanofibres

According to the previous study, the bandgap of g-C_3N_4 is 2.69 eV, and the highest occupied molecular orbital (HOMO) and lowest unoccupied molecular orbital (LUMO) potentials of g-C_3N_4 are –1.12 and 1.57 eV, respectively.[40] Our recent study revealed that the conduction band (CB) and valence band (VB) edge potentials of $TiO_2(B)$ were at -0.33 and 2.72 eV, respectively.[32] As shown in Fig. 7A, the g-C_3N_4 phase could produce photogenerated electron-hole pairs, when the g-C_3N_4/$TiO_2(B)$ nanofibres were exposed to visible light. The electrons generated by visible light are able to transfer to the $TiO_2(B)$ nanofibres through the interface between g-C_3N_4 and $TiO_2(B)$ nanfibres. Given that the photogenerated holes could not transfer to the $TiO_2(B)$ phase due to the more positive VB edge of the $TiO_2(B)$ nanfibres, the overall outcome of the charge transfer was that the electrons transferred to $TiO_2(B)$ nanofibres and the holes was left in the g-C_3N_4 nanoflakes. The separated electrons on the CB of $TiO_2(B)$ nanfibres could be donated to an electron acceptor such as dissolved oxygen leading to formation of $O_2^{\bullet-}$,[41, 42] the holes left on the VB of g-C_3N_4 could react with H_2O directly to yield OH• to oxidise pollutants as well. This phenomenon could efficiently reduce the recombination of the photogenerated electrons and holes, and thus highly improve the photoactivity of the g-C_3N_4/$TiO_2(B)$ nanofibres in visible light range. However, it is hard to form stable heterojunctions between anatase nanofibres and g-C_3N_4 because of the high coincidence site density of g-C_3N_4/$TiO_2(A)$ system. So the photogenerated electrons cannot efficiently transfer to the anatase nanofibres through the heterojunction interface, although the HOMO of g-C_3N_4 is more negative than the CB edge potential of anatase phase. This is the reason why the photoactivity of the g-C_3N_4/$TiO_2(B)$ nanofibres is much higher than that of the g-C_3N_4/$TiO_2(A)$ nanofibres.

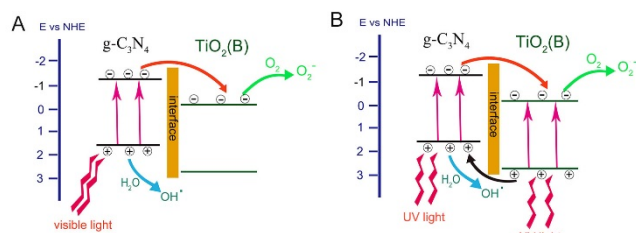**Fig. 7** Proposed charge transfer between g-C_3N_4 and $TiO_2(B)$ nanofibres through the heterjunction interface under visible light irradiation (A) and UV light irradiation (B).

If the g-C_3N_4/$TiO_2(B)$ nanofibres are irradiated by UV light, the valence band electrons in both g-C_3N_4 and $TiO_2(B)$ can be excited. As depicted in Fig. 7B, besides the electron transfer from g-C_3N_4 to $TiO_2(B)$ phase, the photoinduced holes on the surface of $TiO_2(B)$ nanofibres could transfer easily to the g-C_3N_4 nanoflakes through the heterojunctions, since the VB edge potential of $TiO_2(B)$ (2.72 eV) is more positive than the LUMO of g-C_3N_4 (1.57 eV). The photogenerated electrons and holes would aggregate on the surface of g-C_3N_4 flakes and $TiO_2(B)$ nanofibres, respectively. These separated electrons and holes could form reactive oxygen species with O_2 or H_2O, which are responsible for the degradation of dye pollutants. Therefore, compared with pure g-C_3N_4 and $TiO_2(B)$ nanofibres, the photoactivity of g-C_3N_4/$TiO_2(B)$ nanofibres was also improved under UV light irradiation. Unfortunately, the UV light photoactivity of anatase nanofibres decreased with the introduction of g-C_3N_4 (Fig. S2). Firstly, the lack of heterojunctions between g-C_3N_4 and anatase nanofibres could not lead to the efficient separation of the photogenerated charges. On the other hand, the g-C_3N_4 nanoflakes might block the exposure of the anatase nanofibres to the UV light, which will greatly reduce the UV light absorption by the anatase nanofibres.

6 Conclusions

In summary, the g-C_3N_4/$TiO_2(B)$ hybrid photocatalysts were fabricated successfully with the growth of g-C_3N_4 nanoflakes onto the surface of $TiO_2(B)$ nanofibres with exposed (001) plane. According to the TEM investigation, the stable interfacial structure could be formed easily since the plane of (22-40) of g-C_3N_4 and the plane (110) of $TiO_2(B)$ had same *d*-spacing of 0.35 nm and same orientation. This is in good agreement with the results calculated by near coincidence site lattice (NCSL) theory. The stable interfacial structure ensured the g-C_3N_4 nanoflakes were attached firmly onto the surface of $TiO_2(B)$ nanofibres. More importantly, the visible light generated electrons from the g-C_3N_4 nanoflakes could efficiently transfer to the surface of the $TiO_2(B)$ nanofibres via the interfacial structure. So compared with the g-C_3N_4/$TiO_2(B)$ hybrid photocatalysts where interfacial structure was hard to construct, the g-C_3N_4/$TiO_2(B)$ system exhibited better ability for SRB degradation under visible light irradiation. This study proved the significance to form stable interfacial structure in heterojunctions, which is a guide in the search for visible light driven photocatalysts with heterojunctions.

Notes and reference

[a] *College of Chemistry, Chemical and Environmental Engineering; Laboratory of Fiber Materials and Modern Textile, the Growing Base for State Key Laboratory, Qingdao University, Qingdao 266071, China. Tel: 86-532-8595-3361; E-mail: d.yang@qdu.edu.cn; d.yang@griffith.edu.au*
[b] *International Research Center for Renewable Energy, State Key Laboratory of Multiphase Flow in Power Engineering, Xi'an Jiaotong University, Xi'an 710049.*
[c] *Queensland Micro- and Nanotechnology Centre (QMNC), Griffith University, Nathan, Brisbane, QLD 4111, Australia.*
[d] *Material Science and Engineering College, Key Laboratory of Bio-based Material Science and Technology, Ministry of Education, Northeast Forestry University, Harbin 150040, PR China.*
[e] *Institute of Coal Chemistry, CAS, Taiyuan, 030001, PR China. Email: zfzheng@sxicc.ac.cn*

† Electronic Supplementary Information (ESI) available: TEM

image of TiO$_2$(B) and anatase nanofibres, calculation of the orientation relations between TiO$_2$(B) and g-C$_3$N$_4$ by using near coincidence site lattice (NCSL) theory, photoactivity of g-C$_3$N$_4$/TiO$_2$(A) nanofibres under UV light irradiation.

1. M. R. Hoffmann, S. T. Martin, W. Choi and D. W. Bahnemann, *Chem. Rev.*, 1995, **95**, 69.
2. T. L. Thompson and J. T. Yates Jr, *Chem. Rev.*, 2006, **106**, 4428.
3. A. L. Linsebigler, G. Lu and J. T. Yates Jr, *Chem. Rev.*, 1995, **95**, 735.
4. M. Anpo and M. Takeuchi, *Int. J. Photoenergy*, 2001, **3**, 89.
5. A. D. Paola, S. Ikeda, G. Marcì, B. Ohtani and L. Palmisano, *Int. J. Photoenergy*, 2001, **3**, 171.
6. C. C. Hu, T. C. Hsu and L. H. Kao, *Int. J. Photoenergy*, 2012, **2012**, 391958.
7. X. B. Chen and S. S. Mao, *Chem. Rev.*, 2007, **107**, 2891.
8. T. C. An, J. X. Chen, G. Y. Li, X. J. Ding, G. Y. Sheng, J. M. Fu, B. X. Mai and K. E. O'Shea, *Catal. Today*, 2008, **139**, 69.
9. S. S. Zhao, S. Chen, H. T. Yu and X. Quan, *Sep. Purif. Technol.*, 2012, **99**, 50.
10. T. Ohno, M. Akiyoshi, T. Umebayashi, K. Asai, T. Mitsui and M. Matsumura, *Appl. Catal. A Gen.*, 2004, **265**, 115.
11. Y. V. Kolen'Ko, A. V. Garshev, B. R. Churagulov, S. Boujday, P. Portes and C. Colbeau-Justin, *J. Photochem. Photobiol. A: Chem.*, 2005, **172**, 19.
12. A. Naldoni, M. Allieta, S. Santangelo, M. Marelli, F. Fabbri, S. Cappelli, C. L. Bianchi, R. Psaro and V. Dal Santo, *J. Am. Chem. Soc.*, 2012, **134**, 7600.
13. X. Chen, L. Liu, Y. Y. Peter and S. S. Mao, *Science*, 2011, **331**, 746.
14. M. Anpo, Y. Ichihashi, M. Takeuchi and H. Yamashita, *Res. Chem. Intermed.*, 1998, **24**, 143.
15. M. Anpo and M. Takeuchi, *J. Catal.*, 2003, **216**, 505.
16. M. Takeuchi, H. Yamashita, M. Matsuoka, M. Anpo, T. Hirao, N. Itoh and N. Iwamoto, *Catal. Lett.*, 2000, **67**, 135.
17. H. Yamashita, M. Harada, J. Misaka, M. Takeuchi, B. Neppolian and M. Anpo, *Catal. Today*, 2003, **84**, 191.
18. M. Ni, M. K. Leung, D. Y. Leung and K. Sumathy, *Renew. Sust. Energy. Rev.*, 2007, **11**, 401.
19. R. Asahi, T. Morikawa, T. Ohwaki, K. Aoki and Y. Taga, *Science*, 2001, **293**, 269.
20. S. U. Khan, M. Al-Shahry and W. B. Ingler, *Science*, 2002, **297**, 2243.
21. K. Kobayakawa, Y. Murakami and Y. Sato, *J. Photochem. Photobiol. A: Chem.*, 2005, **170**, 177.
22. M. Okada, Y. Yamada, P. Jin, M. Tazawa and K. Yoshimura, *Thin Solid Films*, 2003, **442**, 217.
23. G. R. Torres, T. Lindgren, J. Lu, C. G. Granqvist and S. E. Lindquist, *J. Phys. Chem. B*, 2004, **108**, 5995.
24. J. Zhang, Y. Wu, M. Xing, S. A. K. Leghari and S. Sajjad, *Energ. Environ. Sci.*, 2010, **3**, 715.
25. D. J. Yang, C. C. Chen, Z. F. Zheng, H. W. Liu, E. R. Waclawik, Z. M. Yan, Y. N. Huang, H. J. Zhang, J. C. Zhao and H. Y. Zhu, *Energ. Environ. Sci.*, 2011, **4**, 2279.
26. R. Zhu, C. Y. Jiang, B. Liu and S. Ramakrishna, *Adv. Mater.*, 2009, **21**, 994.
27. T. X. Wu, G. M. Liu, J. C. Zhao, H. S. Hidaka and N. Serpone, *J. Phys. Chem. B*, 1998, **102**, 5845.
28. D. Chatterjee and A. Mahata, *Catal. Commun.*, 2001, **2**, 1.
29. R. A. Doong, C. H. Chen, R. Maithreepala and S. M. Chang, *Water Res.*, 2001, **35**, 2873.
30. M. G. Kang, H. E. Han and K. J. Kim, *J. Photochem. Photobiol. A: Chem.*, 1999, **125**, 119.
31. V. Keller and F. Garin, *Catal. Commun.*, 2003, **4**, 377.
32. D. J. Yang, J. Zhao, H. W. Liu, Z. F. Zheng, M. O. Adebajo, H. X. Wang, X. T. Liu, H. J. Zhang, J. C. Zhao, J. Bell and H. Y. Zhu, *Chem. Eur. J.*, 2013.
33. D. J. Yang, H. W. Liu, Z. F. Zheng, Y. Yuan, J. C. Zhao, E. R. Waclawik, X. B. Ke and H. Y. Zhu, *J. Am. Chem. Soc.*, 2009, **131**, 17885.
34. J. Zhang, S. Yan, S. L. Zhao, Q. Xu and C. Li, *Appl. Surf. Sci.*, 2013.
35. H. Y. Zhu, X. P. Gao, Y. Lan, D. Y. Song, Y. X. Xi and J. C. Zhao, *J. Am. Chem. Soc.*, 2004, **126**, 8380.
36. H. Y. Zhu, Y. Lan, X. Gao, S. P. Ringer, Z. Zheng, D. Y. Song and J. C. Zhao, *J. Am. Chem. Soc.*, 2005, **127**, 6730.
37. Y. Lan, X. P. Gao, H. Y. Zhu, Z. F. Zheng, T. Y. Yan, F. Wu, S. P. Ringer and D. Y. Song, *Adv. Funct. Mater.*, 2005, **15**, 1310.
38. C. Pan, J. Xu, Y. Wang, D. Li and Y. Zhu, *Adv. Funct. Mater.*, 2012, **22**, 1518.
39. W. Chen, Z. L. Fan, B. Zhang, G. J. Ma, K. Takanabe, X. X. Zhang and Z. P. Lai, *J. Am. Chem. Soc.*, 2011, **133**, 14896.
40. X. C. Wang, K. Maeda, A. Thomas, K. Takanabe, G. Xin, J. M. Carlsson, K. Domen and M. Antonietti, *Nat. Mater.*, 2008, **8**, 76.
41. K. Ikeda, H. Sakai, R. Baba, K. Hashimoto and A. Fujishima, *J. Phys. Chem. B*, 1997, **101**, 2617.
42. W. Kubo and T. Tatsuma, *J. Am. Chem. Soc.*, 2006, **128**, 16034.